Hindawi
Geofluids
Volume 2022, Article ID 3627654, 14 pages
https://doi.org/10.1155/2022/3627654

Research Article

Study on Microscopic Water Flooding in Porous Carbonate Reservoirs by Numerical Simulation

Tao Yu, Baozhu Li, Mingqiang Hao, and Benbiao Song

Research Institute of Petroleum Exploration and Development, PetroChina, Beijing 100083, China

Correspondence should be addressed to Tao Yu; taoyu001@petrochina.com.cn

Received 21 May 2022; Accepted 2 July 2022; Published 18 July 2022

Academic Editor: Dengke Liu

The study on the flow behaviors of oil and water two phases in porous media and their influencing factor is very important to adjust the porous carbonate reservoir development strategy and enhance the oil recovery. Based on the CT (computed tomography) scanning of real carbonate reservoir core sample, the micropore structure was reconstructed, and the effects of different factors (injection rate, oil-to-water viscosity ratio, and contact angle) and secondary development methods (higher injection rate and water displacement direction optimization) on the flow behavior of oil and water two phases were explored by numerical simulation in this paper. It is found from the study that the pores in the porous carbonate reservoirs have good structural connectivity. During the displacement process, the oil-water interface mainly resides at the pore throat junction with a large change of pore size, and the Haines jumps exist in the oil-water movement; the areal sweep efficiency of the water phase is jointly affected by the viscosity effect, interfacial tension, pore structure, and injection rate. Under the minimum injection rate and oil-to-water viscosity ratio, the maximum oil recovery can be obtained, and the oil recovery is 52.62% and 57.01%, respectively. The recovery efficiency and swept area are better in a water-wet system than oil-wet system. During the secondary development, the remaining oil is hardly displaced even with the injection rate increased by a factor of 50, and it shows improvement after 250 times of initial injection rate. Changing the position of water inlet and the produced fluid outlet results in better recovery since the remaining oil near the new inlet and outlet can be effectively produced.

1. Introduction

In the petroleum industry, oil can be displaced from the formation by water injection. Water flooding is the most commonly used operation measure in the field of oil development [1]. Microscopically, the water flooding process is accompanied by complicated physical behaviors, and the multiphase flow behaviors in porous media are extremely complicated under different forces, such as viscosity force and interfacial tension [2, 3]. Further revelation of the flow behaviors of oil and water two phases in porous media is of great significance in enhancing the oil recovery.

At present, the pore-scale water flooding process is studied mainly by experiments [4, 5] and numerical simulation. In the experiments, two-phase distribution in the process of water flooding was obtained by CT scanning technology and nanochip technology. The numerical simulation method is progressively adopted in the study on oil and water two phases at the pore scale due to its low consumption of resources and ability to control different factors. Different researchers solve the problem of multiphase flow at the pore scale by different mathematical models and methods. What is more, Yang et al. summarized different mathematical models for solving pore-scale multiphase flow problems [6], mainly including the pore network model [7–9], lattice Boltzmann method [10–15], smoothed particle hydrodynamics method [16], finite element method [6, 17], and finite volume method [18, 19].

The finite volume method is used to study the oil and water two-phase flow at pore scale because of its good conservation and applicability for complex geometry [6], mainly including volume of fluid (VOF) methods [20–23], level set methods [24], and phase field (PF) method [25, 26]. Iyi et al. used a volume of fluid model to simulate the transport process of oil and water two phases in pore channels and considered the effects of temperature, contact angle, and

surface tension. The results show that the displacement behaviors of oil- and water-wet systems are greatly affected by oil concentration, and the contact angle significantly affects the oil recovery [27]. Brien et al. constructed a two-dimensional porous medium structure and studied the effects of capillary number and viscosity ratio on pore-scale displacement and the causes and transient dynamics of Haines jumps [28]. Peng et al. used the VOSET (coupled volume of fluid and level set method) method to simulate the water injection process by a reconstructed pore model and analyzed the effects of oil displacement rate and wettability on oil recovery [29]. Pinilla et al. used the CFD (computational fluid dynamics) method to simulate the oil and water two phases in porous media by the VOF model and compared it with the experimentally measured recovery efficiency. Their results show that the absolute error is below 7% [20]. Wang et al. simulated the water flooding process at the pore scale in a nonuniform wettability rock model and analyzed the effects of the critical capillary number on relative permeability, remaining oil recovery efficiency, and immiscible displacement efficiency [17]. Rabbani et al. directly simulated two phases of the liquid-liquid interface in a single capillary channel at high resolution by the OpenFOAM software and discussed the effects of constant fluid velocity and wettability [30]. Liu and Wu discussed the available technologies for pore-scale prediction of immiscible two-phase flow in complicated porous media, numerically simulated the pore fluid flow, and studied the effect of wettability on pore fluid flow accordingly [31]. Aziz et al. used the fluid volume method to study the dynamic two-phase flow, hydrodynamic transport, and wettability alteration in the two-dimensional domain. The numerical simulation results show that after low salinity water injection, (1) the formation brine (i.e., high-salinity water) was swept out from the flowing regions by advection, and (2) the change of wettability potentially influences the increase of recovery efficiency [32]. Minakov et al. studied nanofluid flooding by the fluid volume method based on three-dimensional micromodels for the cores with different permeability and found that the oil recovery increases with increasing mass fraction of nanoparticle [33]. Ning et al. studied the dynamic behaviors of oil-water flow in the pores of low-permeability sandstone reservoirs and the effects of viscosity and capillarity on oil-water flow and found that the viscosity unevenly changes due to the difference in viscosity between oil and water, and the dynamic behaviors of oil and water two-phase flow at the pore scale shown by capillary play a decisive role in the determination of the spatial swept area and ultimate recovery efficiency [34]. Hoang et al. [35] used the VOF method to simulate the slug flow of micro fluid in T-shaped pipe and compared it with the experimental data to verify the effectiveness of VOF method. Yang et al. [36] found that the complex pore structure would lead to the generation of remaining oil, and the phase circulation phenomenon can be observed in the remaining oil and presents two distribution forms: cocurrent driven flow and lid-cavity driven flow.

The above studies focus on the mathematical model algorithm, contact angle, and viscosity ratio. There are few systematic studies on displacement behaviors, especially in porous carbonate reservoirs under different displacement conditions and secondary development schemes. In this paper, a microscopic pore structure model was created by CT scanning of real porous carbonate reservoirs, and numerical simulation was conducted on oil and water two-phase flow in the porous rock accordingly, the author discussed the effects of injection rate, oil-to-water viscosity ratio, wettability, and secondary development schemes in order to provide theoretical explanation and guidance for macroscopic enhancement of oil recovery efficiency from the microscopic point of view.

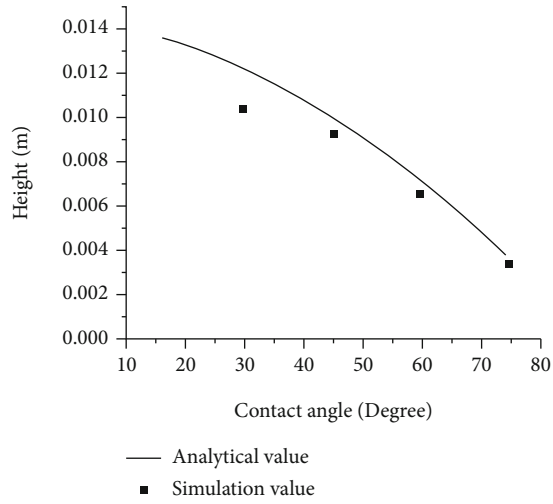

Figure 1: Verification of numerical simulation results.

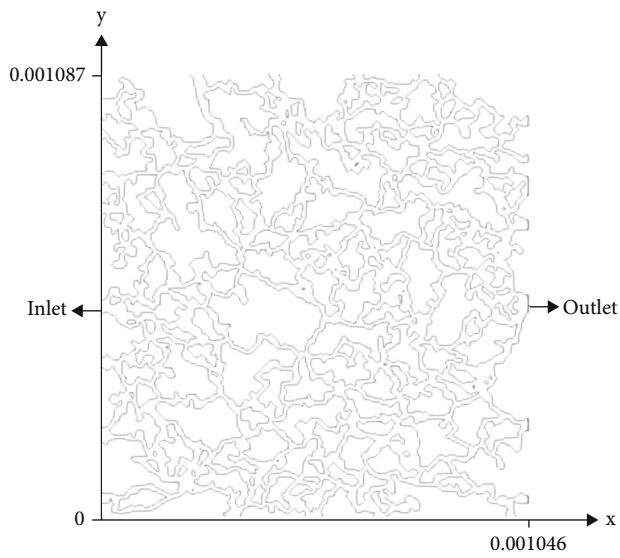

Figure 2: Physical model.

2. Numerical Model Algorithm and Verification

2.1. Numerical Model. The VOF model, a surface tracking method created based on a fixed Eulerian grid, is suitable for tracking the immiscible multiphase flow interface with

Table 1: Case settings.

Case number	Inlet velocity	Oil/water viscosity ratio	Contact angle	Increase velocity	Change injection port position	Purpose
1	0.001 m/s	10	45°	—	—	Influence of different injection rates on two-phase dynamic behavior (TDB)
2	0.005 m/s	10	45°	—	—	
3	0.01 m/s	10	45°	—	—	
4	0.03 m/s	10	45°	—	—	
5	0.05 m/s	10	45°	—	—	
6	0.01 m/s	2	45°	—	—	Influence of different oil-to-water viscosity ratio on TDB
7	0.01 m/s	5	45°	—	—	
8	0.01 m/s	15	45°	—	—	
9	0.01 m/s	20	45°	—	—	
10	0.01 m/s	10	15°	—	—	Influence of different contact angles on TDB
11	0.01 m/s	10	90°	—	—	
12	0.01 m/s	10	135°	—	—	
13	0.01 m/s	10	165°	—	—	
14	0.001 m/s	10	45°	0.05 m/s	—	Influence of increasing the inlet velocity on TDB
15	0.001 m/s	10	45°	0.25 m/s	—	
16	0.001 m/s	10	45°	—	Yes	Influence of changing the inlet and outlet port position on TDB

a clear interface [37]. The Navier-Stokes equation was used to describe the properties of mass conservation and momentum conservation:

$$\nabla \times \boldsymbol{u} = 0, \tag{1}$$

$$\frac{\partial \rho \boldsymbol{u}}{\partial t} + \nabla \times (\rho \boldsymbol{u}\boldsymbol{u}) - \nabla \times (\mu \boldsymbol{\tau}) = -\nabla p_d + \rho \boldsymbol{g}, \tag{2}$$

where ρ is the average density of two phases, μ is the average dynamic viscosity coefficient of two phases, u is the average velocity of two phases, and p_d is the dynamic pressure. The average attribute of the two phases is calculated according to the following equation:

$$\chi = \chi_1 \alpha + (1 - \alpha)\chi_2. \tag{3}$$

χ_1 and χ_2 are the attributes of phase 1 and phase 2, respectively, and α is the volume fraction of phase 1. In the following discussion, phase 1 was the main phase, and phase 2 was the auxiliary phase. The volume fraction of the main phase is explicitly tracked by the following equation during the calculation.

$$\frac{\partial \alpha}{\partial t} + \nabla \times (\boldsymbol{u}\alpha) = 0. \tag{4}$$

Equations (1) and (2) were used to describe the motion process of two phases. The pressure difference on both sides of the two-phase interface can be expressed as:

$$p_1 - p_2 = \sigma k, \tag{5}$$

where σ is the interfacial tension coefficient of two phases and k is the curvature of the interface. The value of k above and below 1 represents the convexity and concavity of the interface, respectively, and is calculated according to the following equation:

$$\mathrm{k} = -\nabla \times \left(\frac{\nabla \alpha}{|\nabla \alpha|} \right). \tag{6}$$

Table 2: Fluid property.

Water	
Density (kg m^{-3})	1000
Viscosity (kg m^{-1} s^{-1})	0.001
Contact angle (°)	45
Oil	
Density (kg m^{-3})	800
Viscosity (kg m^{-1} s^{-1})	0.00148
Tension coefficient (kg s^{-2})	0.07

2.2. Model Discretization. In this study, OpenFOAM (open-source computational fluid dynamics software) is used as a foundational tool to simulate the cases. Equations (1), (2), and (4) are discretized by the finite volume method to obtain the simplified algebraic equations. The PISO (pressure-implicit with splitting of operators) algorithm was used for injection rate and pressure coupling by adaptive time step. The residual error of each physical quantity was set to 10^{-6}, and the maximum Courant number was set to 0.3. The time term, gradient term, divergence term, and Laplace term were resolved by Euler, Gauss linear difference, Gauss vanLeer, and uncorrected Gauss linear difference method, respectively.

Table 3: Boundary condition.

Variable	Physical boundary		
	Inlet	Out	Other
Velocity	FixedValue	ZeroGradient	FixedValue
Pressure	FixedFluxPressure	FixedValue	FixedFluxPressure
Alpha	FixedValue	zeroGradient	constantAlphaContactAngle

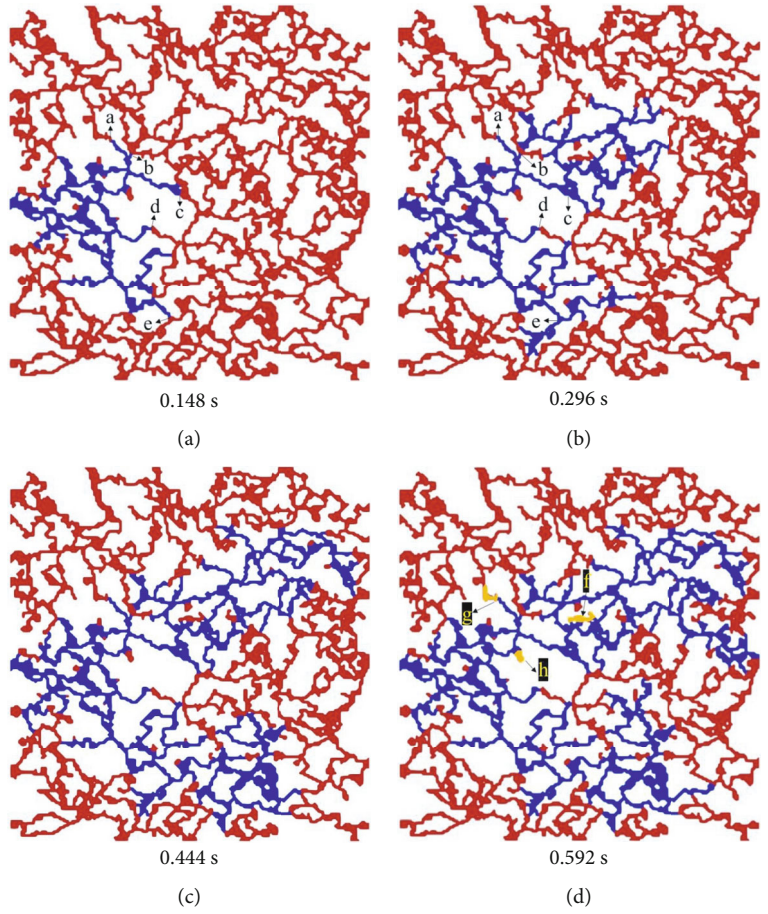

Figure 3: Oil and water two-phase distribution versus time. (a) 0.148 s. (b) 0.296 s. (c) 0.444 s. (d) 0.592 s.

2.3. Validation. When the capillary is placed in water, water will rise along the capillary driven by surface tension, which is a typical flow driven by surface tension. When the final movement is stationary, the rising height of water satisfies the following relationship with the wetting angle, surface tension coefficient, and capillary radius of the capillary:

$$H = \frac{2\sigma \cos\theta}{\rho_w g r}\varphi_f, \tag{7}$$

where θ is the wetting angle, which is used to characterize the wettability of the wall, σ is the interfacial tension coefficient, ρ_w is the density of water, g is gravitational acceleration, and r is the capillary radius. Therefore, the above VOF mathematical model is used to simulate the capillary rise, so as to verify the accuracy of the mathematical model. The calculation domain of this example is a rectangular area with height 2×10^{-2} m and width 10^{-3} m. The total number of grids is 8000.

Figure 1 shows the liquid level height under different wetting angles. It shows that the liquid level height decreases with the increase of wetting angle. The numerical simulation results are similar to the theoretical results, and the values are relatively close. It shows that the mathematical model in this paper can accurately calculate the height of liquid column.

3. Case Setting

3.1. Physical Model and Its Meshing. Figure 2 shows the two-dimensional physical model for pore-scale core used in numerical simulation and calculation after CT scanning,

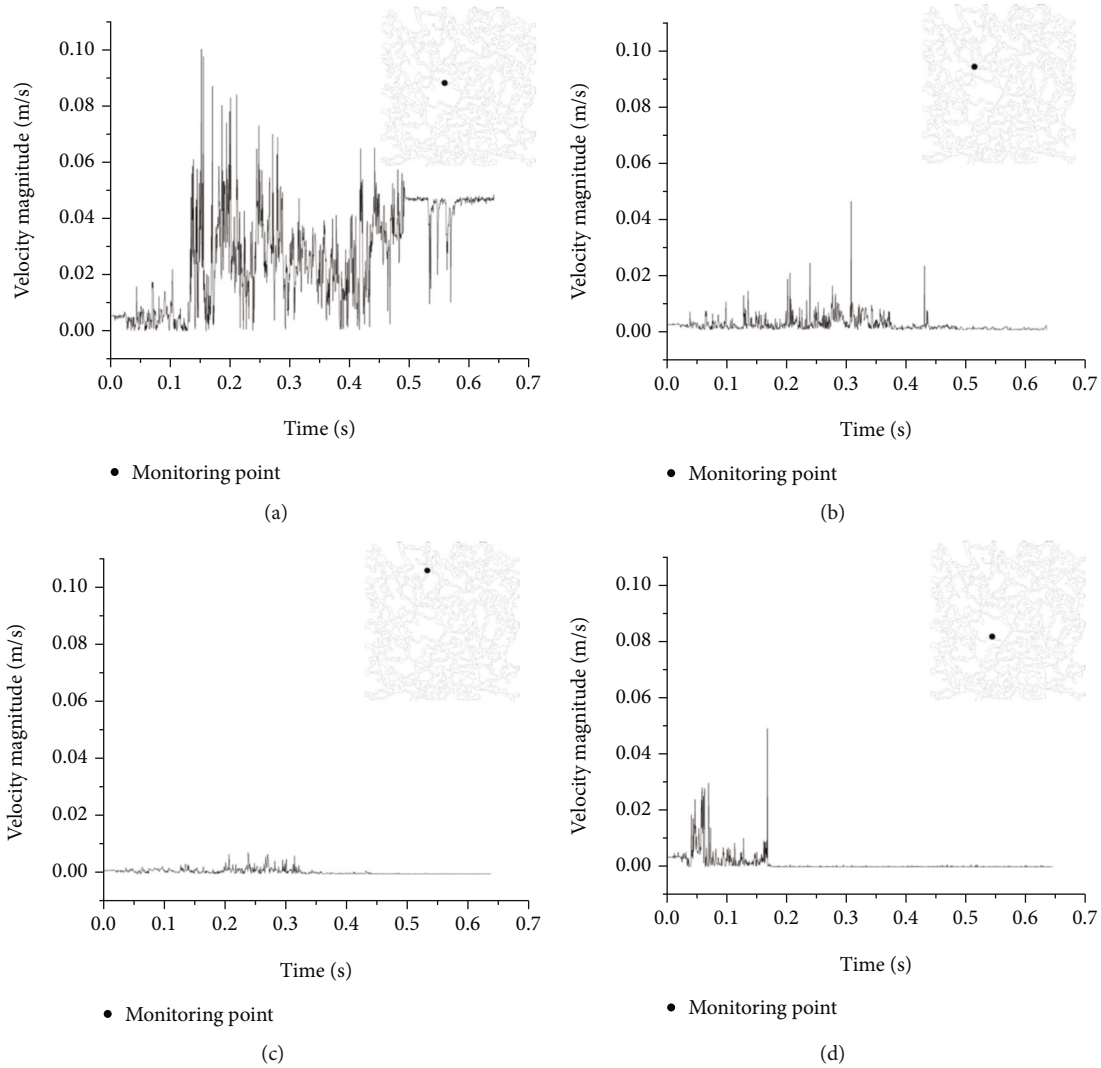

Figure 4: Fluid velocity at different points versus time. (a) Point 1. (b) Point 2. (c) Point 3. (d) Point 4.

image processing, reconstruction, and extraction. The model is 0.001046 m long and 0.001087 m high and has an inlet on the left side and an outlet on the right side, and many micron-scale complicated, tortuous, and interconnected pore channels inside. Water was injected through the water inlet on the middle left and discharged from the outlet on the middle right. The unstructured mesh was used for meshing the physical model, with the 242,654 meshes totally, a minimum mesh volume of $3.1e-17\,\mathrm{m}^3$, and a maximum mesh volume of $3.27e-16\,\mathrm{m}^3$.

3.2. Case Setting. According to the operating conditions and secondary production measures in the oil development process, 16 simulation cases were set, as shown in Table 1. Cases 1~5, 6~9, and 10~13 are the effects of injection velocity, oil-to-water viscosity ratio, and contact angle on oil and water two-phase distribution and recovery efficiency. Cases 14, 15, and 16 are the effects of injection velocity and positions of injection and production wells on oil and water two phases distribution and recovery efficiency.

3.3. Simulation Parameter Setting. The set physical attributes of water and oil in the numerical simulation are shown in Table 2.

The main physical quantities on the physical boundary of the computational domains were set according to the numerical boundary conditions in Table 3. The injection velocity and volume fraction at the inlet, wall, and outlet were set according to the Dirichlet and Neumann boundary conditions. The pressure at the inlet, wall, and outlet was set according to the Neumann and Dirichlet boundary conditions.

4. Result and Discussion

4.1. Transient State

4.1.1. Oil and Water Two-Phase Distribution. Figure 3 shows the oil and water two-phase distribution at different times at the injection velocity of 0.01 m/s. When the injection time is 0.592 s, the water phase flows out of the reservoir stably, and the oil-water two-phase distribution does not change. So, we

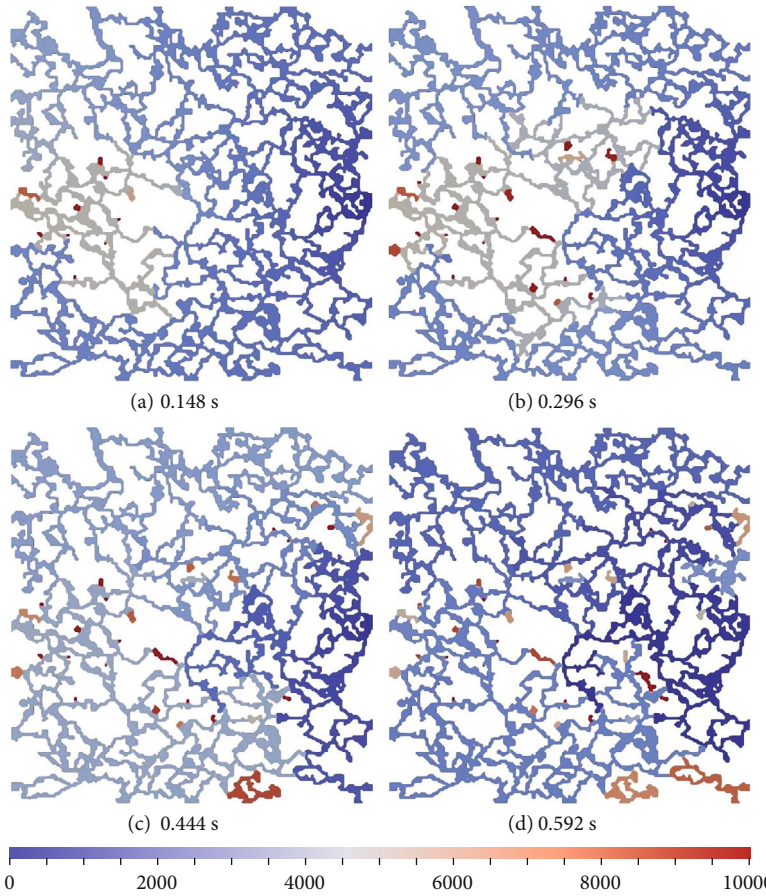

Figure 5: Pressure distribution versus time.

analyze the oil-water two-phase distribution of 0.148 s (0.592 s/4), 0.296 s (0.592 s/2), 0.444 s (3 × 0.592 s/4), and 0.592 s, respectively. At 0.148 s, the water injected from the water inlet on the left displaces upward and downward along the pore channels, with a larger displacement area downward in Figure 3(a). It is worth mentioning that positions a, b, c, d, and e in Figure 3(a) are in the area where the pore throat radius changes greatly mainly due to the sudden change of the pore radius at the junction of pore and throat. When the oil-water interface flows out from the throat on the side of a small radius into the pore on the side of a large radius, the angle between the interface and the wall is above 90°, so the capillary force changes from power to resistance and hinders the movement of the oil-water front. At 0.296 s, the displacement further develops to the right and sweeps the bottom of the reservoir, meaning that the oil at positions c and e at 0.148 s is produced, while the oil at positions a, b, and d cannot be produced further due to the hindrance effect of capillary force unless otherwise at greater displacement pressure. At 0.444 s, upward and downward displacement further develops, resulting in the failure of effective oil displacement in the right middle area. After 0.592 s, the water phase penetrates the reservoir, resulting in the formation of high water cut channels and thus no change of the oil and water two-phase distribution with time. It is worth mentioning that the remaining oil distribution resulting from many different factors forms at the following positions during displacement: (1) area h in Figure 3(d), where the remaining oil is the one at the dead-end formed due to the pore structure; (2) area f in Figure 3(d), where high water cut channels form in the channels on both sides during displacement, resulting in no further displacement of the remaining oil in them, called trap of remaining oil; and (3) area g in Figure 3(d), where the change of the pore structure from small pore to large pore leads to the change of the surface tension direction and hindrance of the water entry to the pore, so the oil phase cannot be produced. In other words, remaining oil forms during water flooding due to complicated and diverse factors, including displacement rate, pore type, and wettability. In short, the water flooding process presents the following characteristics: (1) the water phase unevenly sweeps as proceeds; (2) the oil-water interface stays at the pore throat connection; and (3) the remaining oil can be resulted from dead-end, trapped (bypassed), and pore size change (capillary effect).

4.1.2. Fluid Velocity Change. Figure 4 shows the curve of the fluid velocity at different points versus time at the injection rate of 0.01 m/s. In Figure 4(a), the velocity at Point 1 (0.0004196 m at x-axis and 0.000568 m at y-axis) fluctuates with time, i.e., it fluctuates at a low value at 0~0.14 s, changes

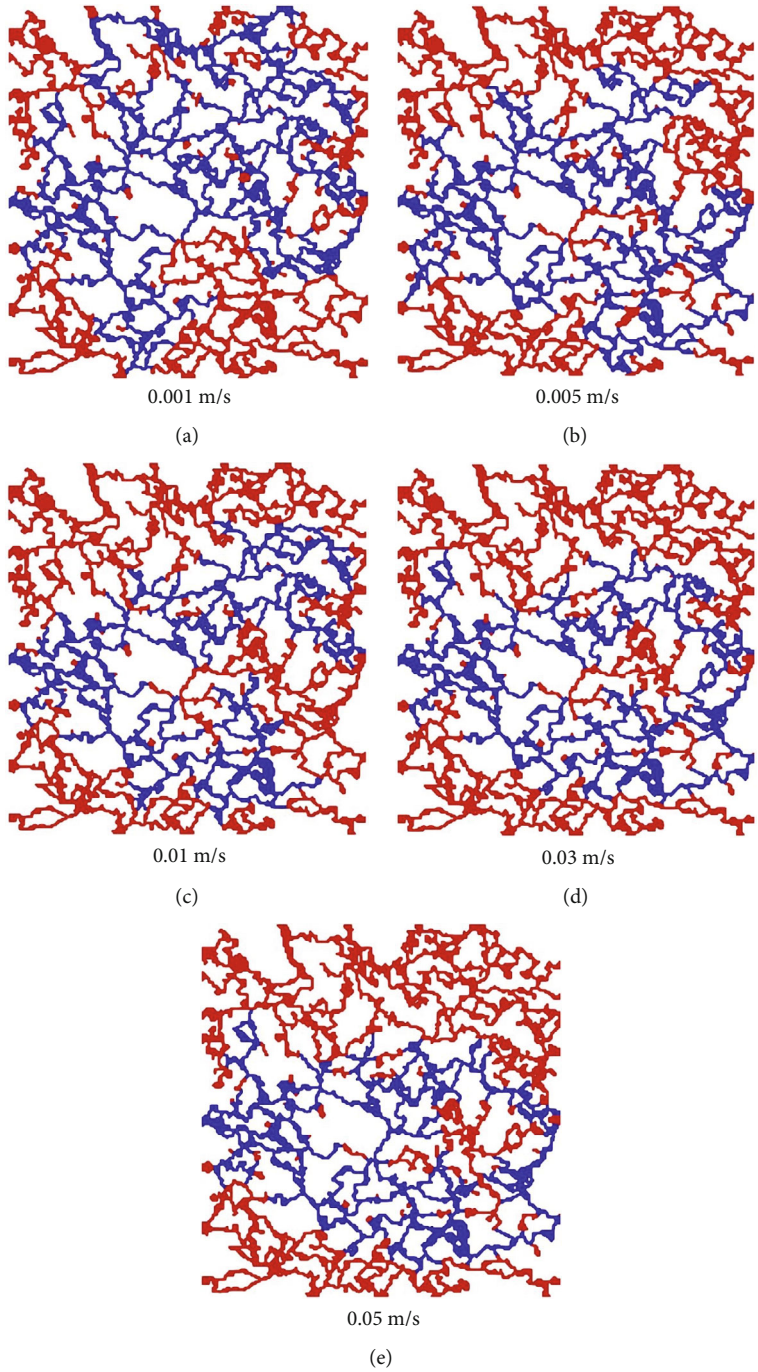

Figure 6: Oil and water two-phase distribution versus injection velocity. (a)0.001 m/s. (b)0.005 m/s. (c)0.01 m/s. (d)0.03 m/s. (e)0.05 m/s.

greatly at 0.14~0.57 s, and changes insignificantly at a high value at 0.57 s~0.7 s mainly because (1) the channel at Point 1 is not the main displacement channel at 0~0.14 s and (2) the channel becomes the main displacement channel at 0.14~0.57 s; when the liquid (water)-liquid (oil) interface moves forward from an irregular channel, the interface shape changes with the cross-sectional dimension of the channel, meaning that the curvature of the interface changes point by point and the capillary pressure on both sides of the interface changes too, so the liquid-liquid interface expands and contracts from time to time and always stays in a transient unbalanced state, meaning that the fluid flows through the porous medium nonuniformly, in the Haines jumps, showing a large jump change of velocity; and (3) a high water cut channel has formed at this point at 0.57 s~0.7 s, i.e., only single-phase (water) flow leads to the change of velocity, so the velocity is high and insignificantly fluctuates. In Figure 4(b), the fluid velocity at Point 2 (0.000356 m at the x-axis and 0.000672 m at the y-axis) fluctuates at a low value at 0~0.38 s and does not change above 0.38 s. It is

worth mentioning that the sudden occurrence of fluid velocity peak at 0.43 s (also at 0.5-0.6 s in Figure 4(a)) may be due to the displacement in other channels affecting the fluid velocity in this channel. In Figure 4(c), the fluid velocity at Point 3 (0.000424 m at the x-axis and 0.000893 m at the y-axis) fluctuates at a low value for a long time, meaning that no oil phase is displaced since the fluid hardly flows in the channel. In Figure 4(d), the velocity at Point 4 (0.000423 m at the x-axis and 0.000434 m at the y-axis) fluctuates at a low value at 0~0.18 s and basically remains 0 above 0.18 s, meaning no displacement in the channel. In a word, the velocity difference in the channel can help to judge the dynamic displacement evolution process and the oil phase production mechanism. Due to different displacement paths, the velocity value is large and changes greatly when the channel is the main displacement channel; and the fluid velocity hardly changes in the pore channels swept by no water phase.

4.1.3. Pressure Distribution. Figure 5 shows the pressure distribution in the reservoir at different times at the injection rate of 0.01 m/s. Figures 5(a)–5(d) shows that the pressure is higher at the inlet and lower at the outlet; with the displacement, the pressure distribution and peak value continuously change. It is found in Figures 3 and 5 that the pressure is much higher in the water phase area than in the oil phase area, directly leading to displacement; with increasing time, the water phase sweeps more area, and the displacement pressure in the reservoir far from the inlet decreases. It is worth mentioning that the displacement pressure in the areas of the above remaining oil zone is high, meaning that these remaining oil can be produced only at greater displacement pressure.

4.2. Influencing Factors

4.2.1. Injection Rate

(1) Oil and Water Two-Phase Distribution. The changes in pressure peak and distribution at different injection rates during displacement directly affect the oil and water two-phase distribution. Figure 6 shows the dynamic effects of injection rate on the oil and water two phases. Figures 6(a)–6(e) show that with increasing injection rate, the swept area decreases; at the lowest injection rate (0.001 m/s), the swept area peaks, and the displacement is relatively uniform at 0.001 m/s, especially in the upper part of the reservoir mainly due to the good pore connectivity. When the displacement power in one channel cannot overcome the interface resistance and viscous effect caused by the change of pore throat, the displacement power in other channels rises, so the remaining oil in other channels is displaced. The cycle of this process results in a more uniform swept area. At higher injection rates (0.03 m/s and 0.05 m/s), water flooding mainly sweeps the middle of the reservoir, and the oil in the upper and lower areas cannot be produced mainly due to several specific channels at a higher injection rate. The displacement pressure can always overcome the viscous force and interfacial tension at a higher injection rate, forming narrow water flooding channels and thus further reduction of the viscous force in the channel (because water has a lower viscosity than oil), more conducive to forward displacement along the channel. This viscous fingering phenomenon has been confirmed by many researchers from experiments and numerical simulations [38–40], when the finger splitting rate increased at higher flow rates leading to low sweeping efficiencies [41].

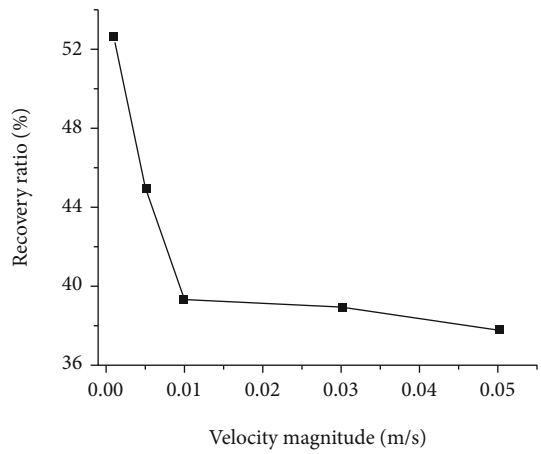

Figure 7: Recovery efficiency versus injection velocity.

(2) Recovery Efficiency. Figure 7 shows the curves of recovery efficiency versus injection rates. It is found that with an increased injection rate, the recovery first decreases and then plateaus. The balance between the viscosity effect and capillary effect at a low injection rate promotes the smooth advancement of the oil-water interface, resulting in the highest recovery efficiency. The viscous effect of fluid dominates at a higher injection rate, so viscous fingering reduces the recovery efficiency. In addition, the pore channel formed by dissolved pores has good homogeneity, strong connectivity, and no drastic change in pore throat ratio; the viscous fingering is not very obvious at a high injection rate (0.03 m/s and 0.05 m/s), so the recovery efficiency declines slightly.

4.2.2. Viscosity

(1) Oil and Water Two-Phase Distribution. Figure 8 is the curve of oil and water two-phase distribution versus oil-to-water viscosity ratio (2, 5, 10, 15, and 20) at the injection rate of 0.01 m/s. It is found from the figure that with increasing oil-to-water viscosity ratio, the waterflood swept area tends towards a decline; at the minimum oil-to-water viscosity ratio of 2, the displacement is complete and uniform, and a large area of remaining oil distributes only in the upper part of the reservoir; at high oil-to-water viscosity ratio (15 and 20), the water flooding paths are mainly around the middle of the reservoir and minorly at the lower left of the reservoir. That is mainly because the movement of oil and water in the rock pores will be affected by the viscous effect. The smaller the oil-to-water viscosity ratio is, the smaller the viscosity force of the fluid calculated according to the Hagen-Poiseuille's equation, meaning the easier displacement in different pore channels, while the higher the oil-to-water

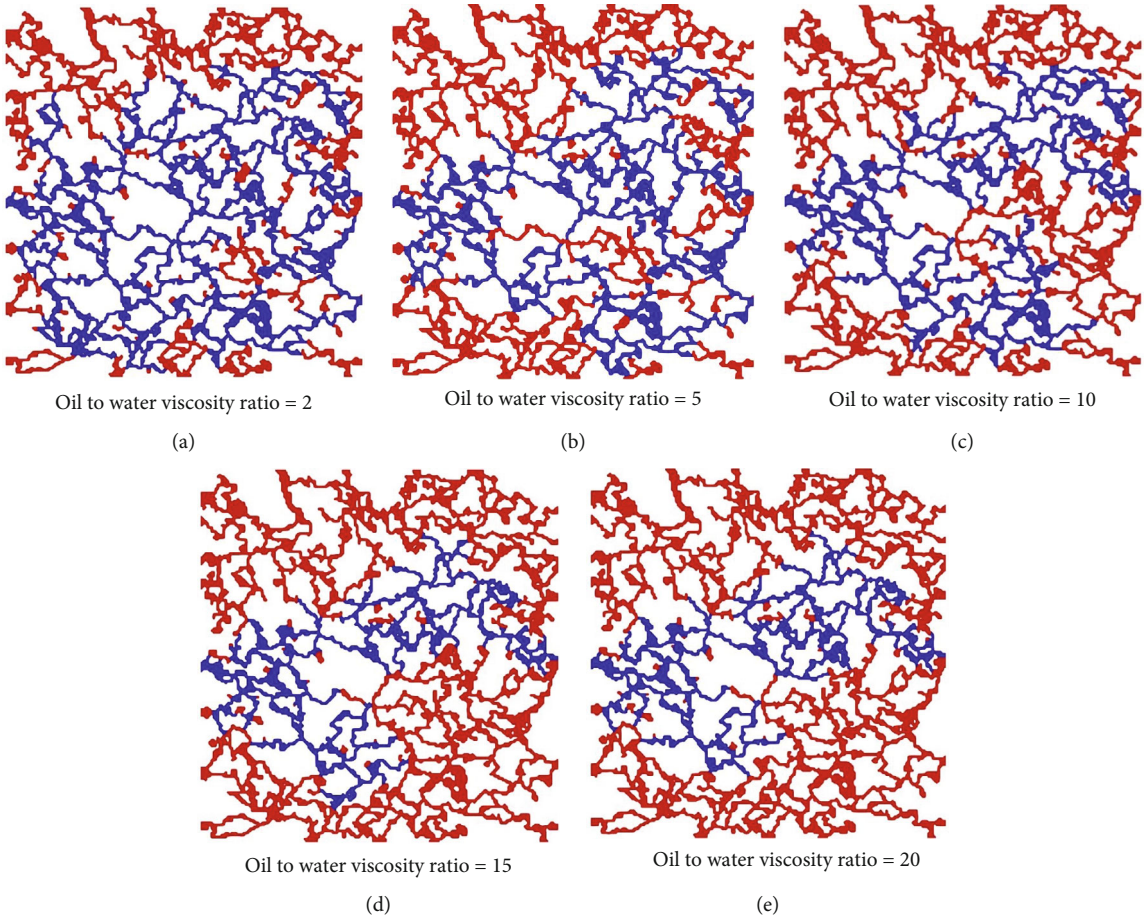

Figure 8: Oil and water two-phase distribution versus viscosity. (a) Oil – to – water viscosity ratio = 2. (b) Oil – to – water viscosity ratio = 5. (c) Oil – to – water viscosity ratio = 10. (d) Oil – to – water viscosity ratio = 15. (e) Oil – to – water viscosity ratio = 20.

viscosity ratio is, the smaller the average viscosity (the viscosity of oil and water calculated according to the volume fraction) in the pore channel of the swept area is, meaning that the displacement is easier in the dominant path and viscous fingering effect forms, resulting in a smaller swept area.

(2) Recovery Efficiency. Figure 9 shows the curve of recovery efficiency versus viscosity. It is found that with increasing oil-to-water viscosity ratio, the recovery efficiency tends towards a decline, consistent with the macroscopic experimental observations. The recovery efficiency is the highest (57.01%) at a low oil-to-water viscosity ratio of 2 and the lowest at high oil-to-water viscosity ratios of 15 and 20, and 44.61% and 39.28% at high oil-to-water viscosity ratio of 5 and 10, respectively. It is worth mentioning that this is consistent with the simulation results of Wei et al. [42].

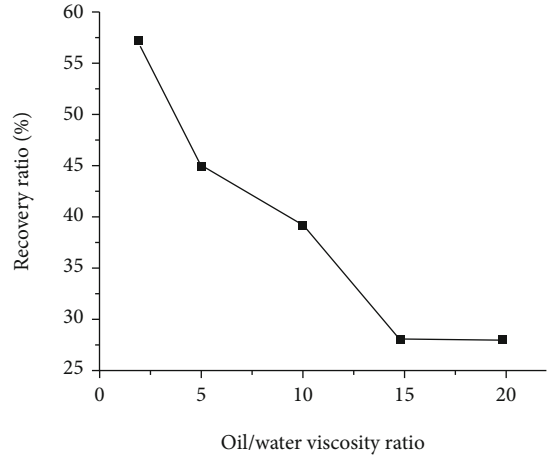

Figure 9: Recovery efficiency versus oil-to-water viscosity ratio.

4.2.3. Contact Angle

(1) Oil and Water Two-Phase Distribution. The analysis of the oil displacement process at different contact angles (15°, 45°, 90°, 135°, and 165°) is conducive to quantitatively evaluating the oil displacement effect of different chemicals in terms of wettability. As shown in Figure 10, the waterflood swept area is significantly greater under water-wet conditions (contact angles of 15° and 45°) than under neutral wet conditions (contact angle of 90°) and oil-wet conditions (contact angles of 135 and 165°); the waterflood swept area includes the lower left and middle areas of the reservoir. In Figure 10(a), the oil-water interface stays at the pore throat interface from the throat to the pore, and water fills the pore

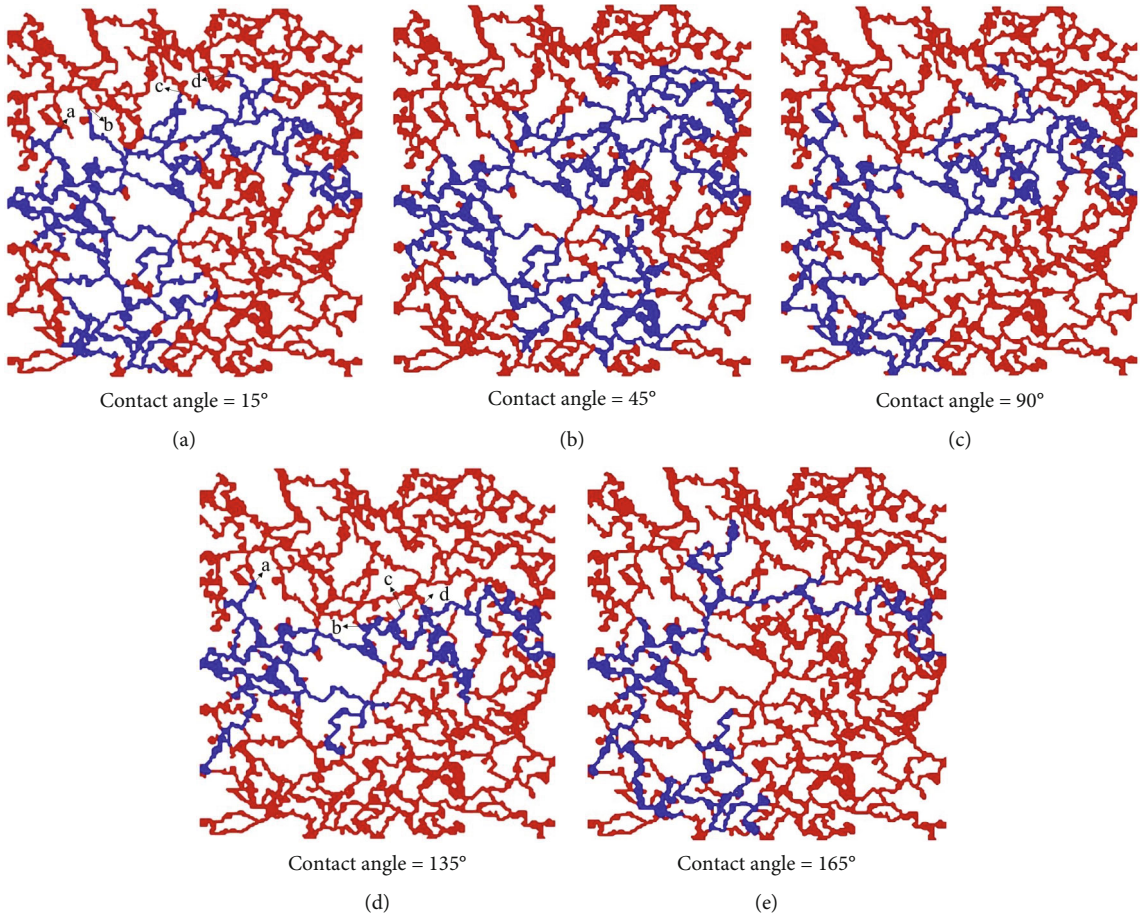

Figure 10: Oil and water two-phase distribution versus contact angle. (a) Contact angle = 15°. (b) Contact angle = 45°. (c) Contact angle = 90°. (d) Contact angle = 135°. (e) Contact angle = 165°.

throat (at Points a, b, c, and d in Figure 10(a)) under the strong water-wet (contact angle of 15°) condition mainly due to the fact that sudden change of pore radius results in the sudden increase of interfacial tension and hindrance of the forward movement of the oil-water interface. In Figure 10(b), a similar phenomenon can be observed at the contact angle of 45°. Under oil-wet conditions (135 and 165°), the oil-water interface stays at the pore throat interface from the pore to the throat, and oil fills the pore throat (Points a, b, c, and d in Figure 10(e)) mainly due to the change of the mechanical state of the capillary at the pore throat interface under oil-wetting conditions. In addition, the waterflood swept area is significantly reduced under oil-wet conditions and especially reduced to only one obvious displacement path in the middle area of the reservoir at the contact angle of 165°. Theoretically, the capillary force is in the same direction as water flooding at the contact angle below 90°, meaning easy displacement, whereas the capillary force is in the opposite direction to water flooding at the contact angle above 90°, meaning that the capillary force shows resistance and thus is not conducive to water flooding.

(2) Recovery Efficiency. Figure 11 shows the oil recovery at different contact angles (15°, 45°, 90°, 135°, and 165°) at the oil-to-water viscosity ratio of 10 and the injection rate of 0.01 m/s. It is found that maximum recovery efficiency is 39.28% at the optimal contact angle (45°); the recovery efficiency is much higher under water-wet conditions than under oil-wet conditions; the recovery efficiency under neutral conditions is 32.04%, between that under water-wet conditions and that under oil-wet conditions.

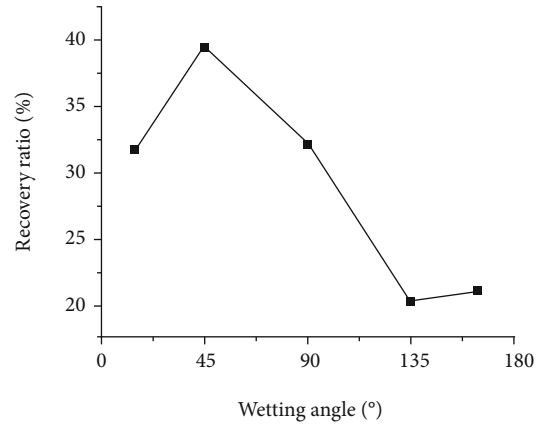

Figure 11: Recovery efficiency versus contact angle.

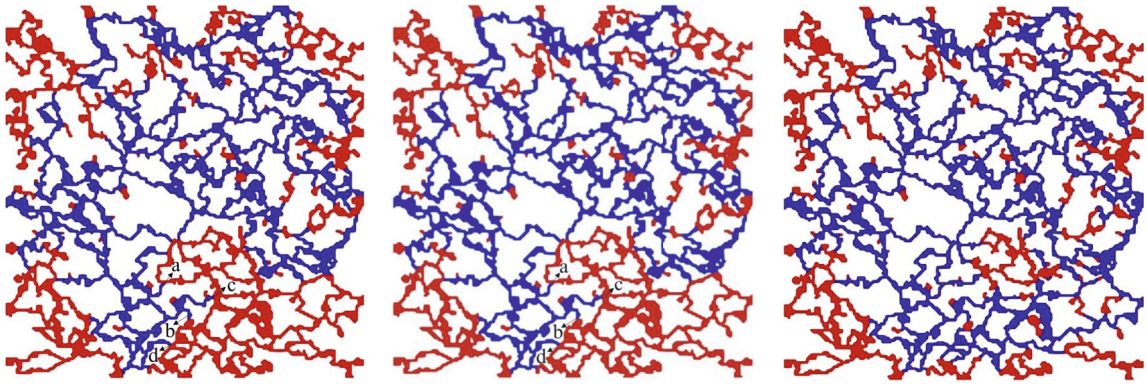

Figure 12: Oil and water two-phase distribution versus injection rate. (a) Original injection rate = 0.001 m/s. (b) Injection rate = 0.05 m/s. (c) Injection rate = 0.25 m/s.

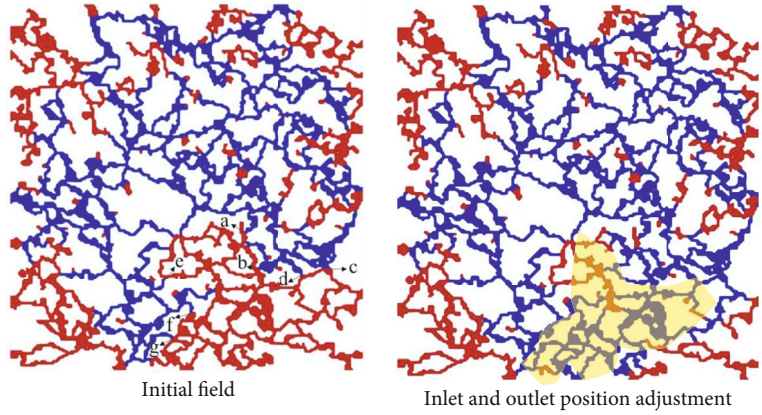

Figure 13: Oil and water two-phase distribution at new inlet and outlet. (a) Initial field. (b) Inlet and outlet position adjustment.

4.3. Secondary Development Methods

4.3.1. Higher Fluid Velocity

(1) Oil and Water Two-Phase Distribution. Intensive injection is commonly seen as an adjustment strategy for the oilfield development improvement at a high water cut stage. In this paper, the dynamic process of oil and water two phases in the reservoir at a higher injection rate was analyzed. Two higher fluid velocities were selected. Water was injected initially at 0.001 m/s to the effluent at the outlet till no significant change in the oil-water two phases with time (Figure 12(a)). The fluid velocity at the inlet was increased to 0.05 m/s (by a factor of 50) and 0.25 m/s (by a factor of 250), respectively. Figures 12(b) and 12(c) show the oil and water two-phase distribution at the higher fluid velocity of 0.05 m/s and 0.25 m/s, respectively. The oil and water two-phase distribution does not change significantly at the fluid velocity of 0.05 m/s. In particular, it is found that the remaining oil at Points a, b, c, and d in Figure 12(a) is not produced, meaning that the displacement pressure generated at the fluid velocity is not enough to overcome the interfacial tension. It is worth mentioning that from Figure 6(e), the remaining oil in the lower middle part of the reservoir is obviously displaced at the injection rate of 0.05 m/s, meaning that the initial oil and water two-phase distribution changes the viscous effect of the whole reservoir gradually from homogeneity to heterogeneity, leading to more difficulties in oil displacement. In addition, the oil phase in the lower part is displaced at the injection rate of 0.25 m/s, meaning that when the injection rate is higher than a certain value, the displacement pressure at the oil-water interface is higher than the capillary resistance formed by the change of pore size, so the oil can be produced.

4.3.2. Injection Production Position Adjustment

(1) Oil and Water Two-Phase Distribution. After the formation of high water cut channels in the reservoir, secondary recovery is carried out by adjusting the positions of the water inlet and produced fluid outlet in addition to the injection rate. As shown in Figure 13, the initial condition is taken as no distribution change of oil and water with time at the injection rate of 0.001 m/s (Figure 13(a)); the water inlet

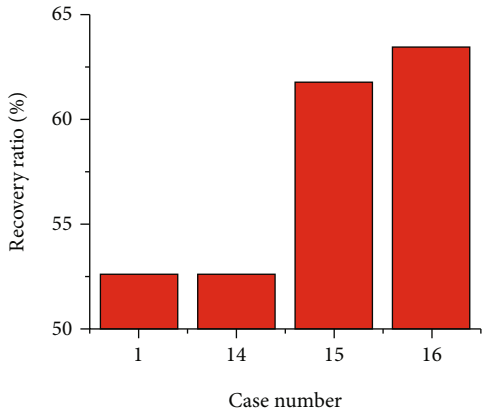

Figure 14: Comparison of the recovery efficiency before and after adjustment of the injection production strategy.

and produced fluid outlet are relocated at the middle upper and lower parts of the reservoir (Figure 13(b)), respectively; accordingly, the injection rate at the new inlet is kept the same as that at the original inlet in order to analyze secondary displacement. It is found in Figures 13(a) and 13(b) that after the relocation of the inlet and outlet, the oil-water interface in the right area of the lower part of the reservoir (Positions a, b, c, and d in Figure 13(a)) is broken through, and the remaining oil in the lower part on the right (yellow area in Figure 13(b)) is produced mainly due to the fact that after relocation, Positions a, b, c, and d are closer to the inlet than Positions e, f, and g, meaning that the displacement pressure is much higher at Points a, b, c, and d than Positions e, f, and g and thus moves forward the displacement interface further. In addition, the remaining oil in other areas is not displaced due to the fact that the interconnected high water cut channels form in the pore throats around the trapped remaining oil, which accounts for a larger fraction of the remaining oil in other areas, and the fluid readily flows along low viscosity force area.

4.3.3. Recovery Efficiency. The following Figure 14 compares the recovery efficiency before and after adjustment of the injection production strategy and quantitative evaluation of the impact of the adjustment. It is found that the recovery efficiency further increases to 61.85% when the injection rate increases by the factor of 250 and does not change when the injection rate increases by the factor of 50. That also means that after primary water flooding at a higher injection rate, an ideal production can be achieved only at a very great injection rate during secondary production in the high water cut stage. In addition, the recovery efficiency can be increased much more significantly to 63.47% by relocating the water inlet and production outlet than by increasing the injection rate.

5. Conclusion

(1) Under interfacial tension and viscous effect, the waterflood sweep in the pore structure is nonuniform. Under interfacial tension, the oil-water interface stays in the area where the pore throat radius changes greatly. The displacement velocity varies significantly in different pore channels, and the water front velocity fluctuates in pulsed way and shows Haines jump

(2) The lower water injection rate results in a larger swept area, and, in turn, higher recovery efficiency while high water injection rate adversely affects the recovery due to viscous fingering. As the injection rate increases from 0.001 m/s to 0.05 m/s, the oil recovery decreases from 52.62% to 37.8%. Additionally, more uniform viscosity ratio between oil and water gives better recovery. When the oil-to-water viscosity ratio is the smallest, the maximum recovery is 57.01%. Considering the wetting conditions, the recovery efficiency is higher under the water-wet than in the neutral and oil-wet conditions

(3) In the secondary recovery scheme, the remaining oil is still not produced when the injection rate is increased by the factor of 50, but the recovery efficiency can be further improved when the injection rate is increased by the factor of 250. After the relocation of the water inlet and produced fluid outlet, the remaining oil near the new inlet and outlet can be effectively produced

Data Availability

The data used to support the finding of this study are available from the corresponding author on reasonable request.

Conflicts of Interest

The authors declare that there is no conflict of interest regarding the publication of this article.

Acknowledgments

This work was supported by the China National Petroleum Corporation Major Technology Project (Grant No. 2021DJ1303).

References

[1] J. Hao, S. Mohammadkhani, H. Shahverdi, M. N. Esfahany, and A. Shapiro, "Mechanisms of smart waterflooding in carbonate oil reservoirs - a review," *Journal of Petroleum Science & Engineering*, vol. 179, pp. 276–291, 2019.

[2] A. Katende and F. Sagala, "A critical review of low salinity water flooding: mechanism, laboratory and field application," *Journal of Molecular Liquids*, vol. 278, pp. 627–649, 2019.

[3] A. Mehmani, R. Verma, and M. Prodanović, "Pore-scale modeling of carbonates," *Marine and Petroleum Geology*, vol. 114, p. 104141, 2020.

[4] J. T. Tetteh, S. E. Cudjoe, S. A. Aryana, and R. B. Ghahfarokhi, "Investigation into fluid-fluid interaction phenomena during low salinity waterflooding using a reservoir-on-a-chip microfluidic model," *Journal of Petroleum Science and Engineering*, vol. 196, p. 108074, 2021.

[5] M. Mohammadi, H. Nikbin-Fashkacheh, and H. Mahani, "Pore network-scale visualization of the effect of brine composition on sweep efficiency and speed of oil recovery from carbonates using a photolithography-based calcite microfluidic model," *Journal of Petroleum Science and Engineering*, vol. 208, p. 109641, 2022.

[6] Y. Yang, K. Wang, Q. Lv et al., "Flow simulation considering adsorption boundary layer based on digital rock and finite element method," *Petroleum Science*, vol. 18, no. 1, pp. 183–194, 2021.

[7] W. Song, J. Yao, D. Wang, Y. Li, H. Sun, and Y. Yang, "Dynamic pore network modelling of real gas transport in shale nanopore structure," *Journal of Petroleum Science and Engineering*, vol. 184, p. 106506, 2020.

[8] Y. Yang, K. Wang, L. Zhang, H. Sun, K. Zhang, and J. Ma, "Pore-scale simulation of shale oil flow based on pore network model," *Fuel*, vol. 251, pp. 683–692, 2019.

[9] M. Piri and M. J. Blunt, "Three-dimensional mixed-wet random pore-scale network modeling of two-and three-phase flow in porous media," *I. Model description. Physical Review E*, vol. 71, no. 2, p. 026301, 2005.

[10] M. Tang, S. Lu, H. Zhan, G. Wenqjie, and H. Ma, "The effect of a microscale fracture on dynamic capillary pressure of two-phase flow in porous media," *Advances in Water Resources*, vol. 113, pp. 272–284, 2018.

[11] Y. Yang, Z. Liu, J. Yao et al., "Flow simulation of artificially induced microfractures using digital rock and lattice Boltzmann methods," *Energies*, vol. 11, no. 8, p. 2145, 2018.

[12] Z. Yang, Y. Méheust, I. Neuweiler, R. Hu, A. Niemi, and Y. F. Chen, "Modeling immiscible two-phase flow in rough fractures from capillary to viscous fingering," *Water Resources Research*, vol. 55, no. 3, pp. 2033–2056, 2019.

[13] L. Zhang, C. Zhang, K. Zhang et al., "Pore-scale investigation of methane hydrate dissociation using the lattice Boltzmann method," *Water Resources Research*, vol. 55, no. 11, pp. 8422–8444, 2019.

[14] J. Zhao, J. Yao, A. Li et al., "Simulation of microscale gas flow in heterogeneous porous media based on the lattice Boltzmann method," *Journal of Applied Physics*, vol. 120, no. 8, p. 084306, 2016.

[15] T. Akai, M. J. Blunt, and B. Bijeljic, "Pore-scale numerical simulation of low salinity water flooding using the lattice Boltzmann method," *Journal of Colloid and Interface Science*, vol. 566, pp. 444–453, 2020.

[16] Q. Yang, J. Yao, Z. Huang, G. Zhu, L. Liu, and W. Song, "Pore-scale investigation of petro-physical fluid behaviours based on multiphase SPH method," *Journal of Petroleum Science and Engineering*, vol. 192, p. 107238, 2020.

[17] Y. Wang, R. Song, J. J. Liu, M. M. Cui, and P. G. Ranjith, "Pore scale investigation on scaling-up micro-macro capillary number and wettability on trapping and mobilization of residual fluid," *Journal of contaminant hydrology*, vol. 225, p. 103499, 2019.

[18] M. Alizadeh and M. Fatemi, "Mechanistic study of the effects of dynamic fluid/fluid and fluid/rock interactions during immiscible displacement of oil in porous media by low salinity water: direct numerical simulation," *Journal of Molecular Liquids*, vol. 322, p. 114544, 2021.

[19] M. Shams, A. Q. Raeini, M. J. Blunt, and B. Bijeljic, "A numerical model of two-phase flow at the micro-scale using the volume-of- fluid method," *Journal of Computational Physics*, vol. 357, pp. 159–182, 2018.

[20] A. Pinilla, L. Ramirez, M. Asuaje, and N. Ratkovich, "Modelling of 3D viscous fingering: Influence of the mesh on core-flood experiments," *Fuel*, vol. 287, p. 119441, 2021.

[21] A. Q. Raeini, B. Bijeljic, and M. J. Blunt, "Modelling capillary trapping using finite-volume simulation of two-phase flow directly on micro-CT images," *Advances in Water Resources*, vol. 83, pp. 102–110, 2015.

[22] T. Shende, V. Niasar, and M. Babaei, "Pore-scale simulation of viscous instability for non-Newtonian two-phase flow in porous media," *Journal of Non-Newtonian Fluid Mechanics*, vol. 296, p. 104628, 2021.

[23] A. Q. Raeini, M. J. Blunt, and B. Bijeljic, "Modelling two-phase flow in porous media at the pore scale using the volume- of-fluid method," *Journal of Computational Physics*, vol. 231, no. 17, pp. 5653–5668, 2012.

[24] A. Ferrari, M. Magnini, and J. R. Thome, "A flexible coupled level set and volume of fluid (flexCLV) method to simulate microscale two-phase flow in non-uniform and unstructured meshes," *International Journal of Multiphase Flow*, vol. 91, pp. 276–295, 2017.

[25] L. Zhang, C. Xu, Y. Guo et al., "The effect of surface roughness on immiscible displacement using pore scale simulation," *Transport in Porous Media*, vol. 140, no. 3, pp. 713–725, 2021.

[26] G. Zhu, J. Kou, J. Yao, A. Li, and S. Sun, "A phase-field moving contact line model with soluble surfactants," *Journal of Computational Physics*, vol. 405, p. 109170, 2020.

[27] D. Iyi, Y. Balogun, B. Oyeneyin, and N. Faisal, "Numerical modelling of the effect of wettability, interfacial tension and temperature on oil recovery at pore-scale level," *Journal of petroleum science and engineering*, vol. 201, p. 108453, 2021.

[28] A. O'Brien, S. Afkhami, and M. Bussmann, "Pore-scale direct numerical simulation of Haines jumps in a porous media model," *European Physical Journal-Special Topics*, vol. 229, no. 10, pp. 1785–1798, 2020.

[29] J. Peng, R. Song, Y. Wang, and H. Xiao, "Comparative study of VOF, LS, and VOSET on pore-scale immiscible waterflooding modeling," *Petroleum*, vol. 7, no. 3, pp. 314–324, 2021.

[30] H. S. Rabbani, V. J. Niasar, and N. Shokri, "Effects of intermediate wettability on entry capillary pressure in angular pores," *Journal of Colloid and Interface Science*, vol. 473, pp. 34–43, 2016.

[31] Z. Liu and H. Wu, "Pore-scale modeling of immiscible two-phase flow in complex porous media," *Applied Thermal Engineering*, vol. 93, pp. 1394–1402, 2016.

[32] R. Aziz, V. Joekar-Niasar, P. J. Martínez-Ferrer, O. E. Godinez-Brizuela, C. Theodoropoulos, and H. Mahani, "Novel insights into pore-scale dynamics of wettability alteration during low salinity waterflooding," *Scientific reports*, vol. 9, no. 1, pp. 1–13, 2019.

[33] A. V. Minakov, D. V. Guzei, M. I. Pryazhnikov, S. A. Filimonov, and Y. O. Voronenkova, "3D pore-scale modeling of nanofluids-enhanced oil recovery," *Petroleum Exploration and Development*, vol. 48, no. 4, pp. 956–967, 2021.

[34] T. Ning, M. Xi, B. Hu, L. Wang, C. Huang, and J. Su, "Effect of viscosity action and capillarity on pore-scale oil-water flowing behaviors in a low-permeability sandstone waterflood," *Energies*, vol. 14, no. 24, pp. 8200–8230, 2021.

[35] D. A. Hoang, V. van Steijn, L. M. Portela, M. T. Kreutzer, and C. R. Kleijn, "Benchmark numerical simulations of segmented two-phase flows in microchannels using the volume of fluid method," *Computers & Fluids*, vol. 86, no. 7, pp. 28–36, 2013.

[36] Y. Yang, S. Cai, J. Yao et al., "Pore-scale simulation of remaining oil distribution in 3D porous media affected by wettability and capillarity based on volume of fluid method," *International Journal of Multiphase Flow*, vol. 143, p. 103746, 2021.

[37] C. W. Hirt and B. D. Nichols, "Volume of fluid (VOF) method for the dynamics of free boundaries," *Journal of Computational Physics*, vol. 39, no. 1, pp. 201–225, 1981.

[38] M. Mishra, P. M. J. Trevelyan, C. Almarcha, and A. De Wit, "Influence of double diffusive effects on miscible viscous fingering," *Physical review letters*, vol. 105, no. 20, p. 204501, 2010.

[39] M. Belotserkovskaya and A. Konyukhov, "Numerical simulation of viscous fingering in porous media," *Physica Scripta*, vol. 2010, no. T142, p. 014056, 2010.

[40] Y. F. Chen, S. Fang, D. S. Wu, and R. Hu, "Visualizing and quantifying the crossover from capillary fingering to viscous fingering in a rough fracture," *Water Resources Research*, vol. 53, no. 9, pp. 7756–7772, 2017.

[41] A. Pinilla, M. Asuaje, and N. Ratkovich, "Experimental and computational advances on the study of viscous fingering: an umbrella review," *Heliyon*, vol. 7, no. 7, p. e07614, 2021.

[42] X. X. Wei, Q. H. Feng, X. M. Zhang, Y. S. Huang, and L. J. Liu,, "Distribution of remaining oil in water flooding at pore scale: volume of fluid method," *Chinese Journal of Computational Physics*, vol. 38, no. 5, pp. 573–584, 2021.